ACS NANO

www.acsnano.org

ARTICLE

Electrostatic Jumping of Frost

Ranit Mukherjee, S. Farzad Ahmadi, Hongwei Zhang, Rui Qiao, and Jonathan B. Boreyko*

Cite This: *ACS Nano* 2021, 15, 4669–4677

Read Online

ACCESS | Metrics & More | Article Recommendations | Supporting Information

ABSTRACT: **The electrification of ice has been a subject of research since 1940, mostly in the context of charge generation in thunderstorms. This generation of electric charge is spontaneous, distinct from applying an external electric field to affect the diffusive growth of ice crystals. Here, we exploit the spontaneous electrification of ice to reveal a surprising phenomenon of jumping frost dendrites. We use side-view high-speed imaging to experimentally observe frost dendrites breaking off from mother dendrites and/or the substrate to jump out-of-plane toward an opposing polar liquid. Analytical and numerical models are then developed to estimate the attractive force between the frost dendrites and liquid, in good agreement with the experimental results. These models estimate the extent of charge separation within a growing sheet of frost, which is caused by mismatches in the mobilities of the charge carriers in ice. Our findings show that the unexpected jumping frost event can serve as a model system for resolving long-standing questions in atmospheric physics regarding charge separation in ice, while also having potential as a deicing construct.**

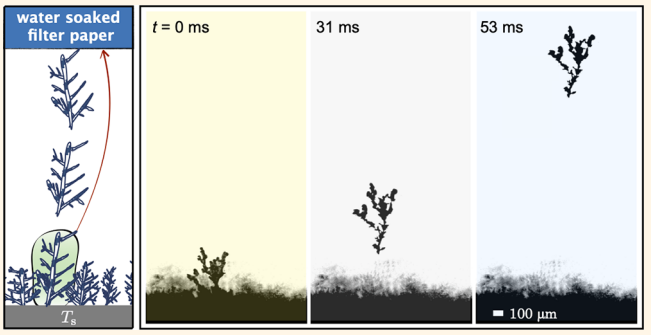

KEYWORDS: *condensation frosting, deicing, electrostatic force, electric polarization, ionic transport, jumping frost*

If we bring an electrically charged rod near a water faucet, the stream of water gets deflected. This simple childhood experiment shows us the remarkable dipolar nature of water molecules, which become partially aligned in the presence of an electric field.[1] Hexagonal ice, on the other hand, cannot exhibit a net alignment even in an electric field.[2] However, colliding ice particles can acquire an electric charge due to a difference in contact potentials.[3] Further, charge separation can occur across ice that exhibits a temperature gradient,[4−6] such that a particle broken off the ice can exhibit a net charge. For example, when air is blown over frost grown on a cold substrate, microscale "splinters" of ice get caught in the flow which exhibit a negative electric charge.[7−9] Similarly, when a frosted sphere was placed within a humid air flow, frost dendrites were observed to detach into the flow and even explode into multiple pieces.[10] When frost is grown on a wire set at a high voltage, simulating the conditions during a thunderstorm, it can generate charged ice splinters[11−13] or even water droplets.[14]

These previous reports clearly demonstrated that ejected ice particles can carry a charge; however, either a convective air flow[7−10] or high voltage[11,12,14] was required to cause the ejection. Here, we demonstrate that not only splinters of frost but entire frost dendrites can break off and jump from a growing frost sheet solely in the presence of an opposing water film or droplet (Figure 1a,b). No air flow or applied voltage was required, such that the jumping dynamics could be noninvasively captured with high-speed photography. We show that the attractive force between the frost dendrites and body of water can be extracted from the jumping kinematics and compared to models of charge separation in frost.

RESULTS AND DISCUSSION

Experimental Setup. Our experimental setup involves growing frost on a substrate and placing a liquid droplet or film at some height above the substrate (Figure 2a,b). We used a completely dry hydrophobic silicon wafer, which was thermally bonded to a Peltier stage set at $T_s = -10 \pm 1$ °C within a room-temperature environment (air temperature $T_\infty = 25 \pm 0.5$ °C and relative humidity RH = 40 ± 10%). To suspend water above the silicon substrate, a 2 cm × 2 cm filter paper was attached to a 3D-printed holder that was connected to a syringe pump (see Figure S1 in the Supporting Information). The out-of-plane gap between the silicon and wetted paper was varied as H = 1, 2.5, or 5 mm. Initially, the filter paper remained dry, while frost grew on the chilled substrate *via* condensation frosting.[15] When the frost sheet grew to a desired

Received: November 2, 2020
Accepted: February 2, 2021
Published: February 24, 2021

https://dx.doi.org/10.1021/acsnano.0c09153
ACS Nano 2021, 15, 4669–4677

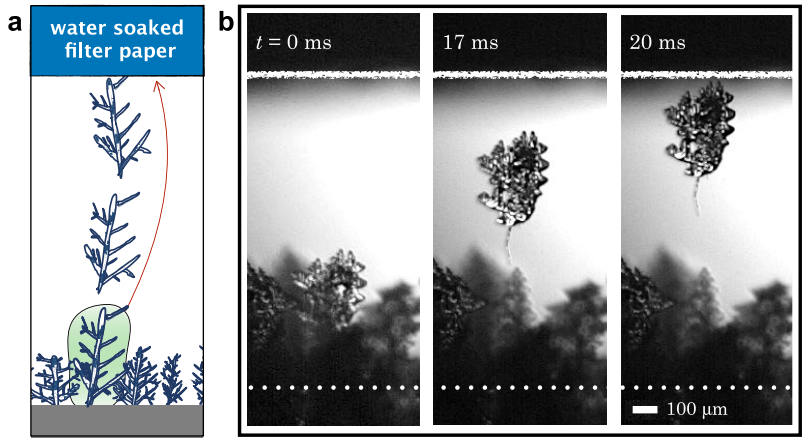

Figure 1. Jumping frost phenomenon. (a) When a wet piece of paper is brought above a growing sheet of frost, frost dendrites can break off from the sheet and jump toward the paper. (b) Experimental chronophotograph of a jumping frost event, where an entire frost dendrite detached from its substrate to jump toward a wet filter paper. The dotted line at the bottom visualizes the top face of the substrate from which the frost was grown.

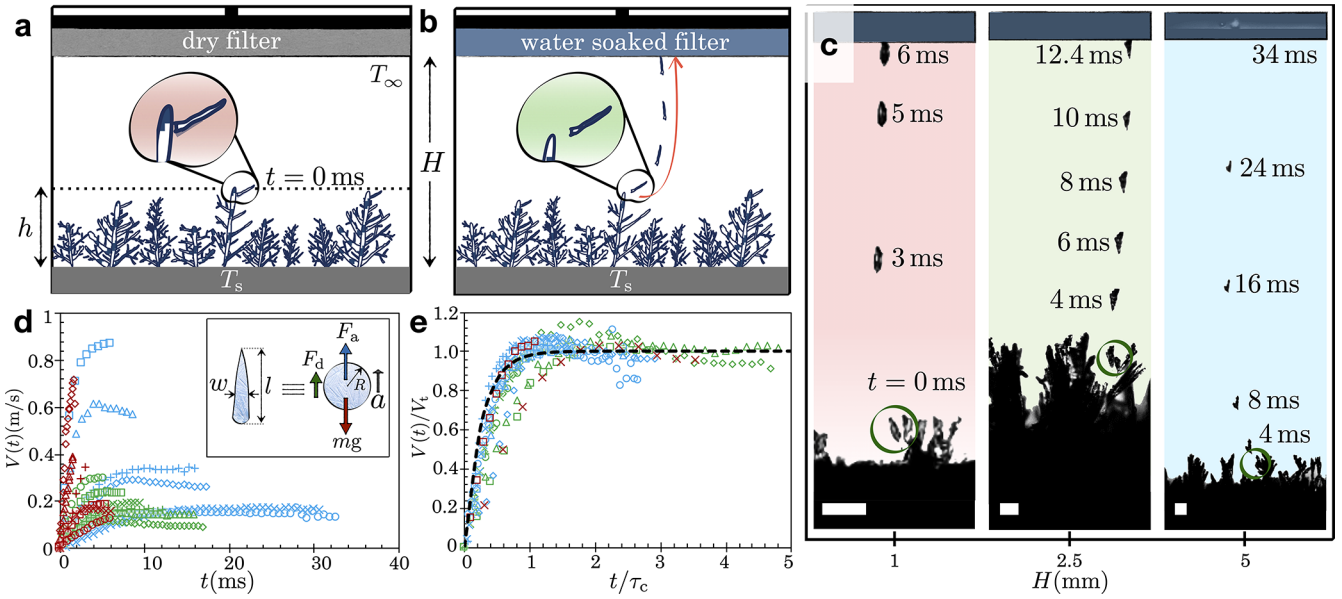

Figure 2. Dynamics of the jumping frost. (a) Schematic of the experiment: frost was grown to an average height h on a subzero temperature (T_s) substrate. A filter paper was suspended at a variable height H above the frosted substrate. (b) Shortly after adding water to the filter paper, frost particles broke off and jumped toward the water-soaked paper. (c) Chronophotography of a micrometric jumping frost particle, from the instance of break-off ($t = 0$) until it reaches the wet filter paper, for three different cases of H = 1 mm (red), 2.5 mm (green), and 5 mm (blue). All scale bars represent 100 μm. (d) Dimensional plot of jumping velocity *vs* time for frost particles jumping toward the suspended wet filter paper. The color scheme of the data points matches that of (c). Different symbols within a color scheme represent separate trials. (Inset) Free body diagram of the spherical approximation of an irregularly shaped dendrite. (e) Equivalent nondimensional plot, where all data collapse onto a universal theory line.

thickness, typically in the range of $h \approx 120-800$ μm, approximately 100 μL of water was dispensed onto the filter paper (Figure 2b). As soon as the paper became saturated with water, several of the dendrites within the frost sheet began to twist and turn.

Periodically, one or more of the micrometric dendritic branches or "splinters" would break off from the frost sheet and jump toward the wetted paper (Figure 2c). Jumping dendrites exhibited an initial acceleration on the order of $a \approx$ 10 g and traversed the gap within $t \approx 1-10$ ms. These jumping events tended to begin around ~10 s after wetting the paper and continued intermittently until the frost growth began to taper off. This jumping frost effect was also observed on hydrophilic glass and a superhydrophilic aluminum hydroxide surface, indicating that the phenomenon can occur over a wide variety of surface wettabilities and irrespective of differences in the thermal and electrical conductivities (see Figure S2b,c and Movie 1). As micrometric frost splinters jumped with greater frequency than entire (millimetric) dendrites, while also exhibiting a simpler shape, we focus our attention on the splinters as a model system to understand the mechanisms behind the jumping phenomenon. At the same time, the analysis will remain conceptually valid for the more dramatic case of whole frost dendrite jumping.

Dynamics of Jumping Frost. The velocities of the jumping frost were plotted against time for different H (Figure

https://dx.doi.org/10.1021/acsnano.0c09153
ACS Nano 2021, 15, 4669−4677

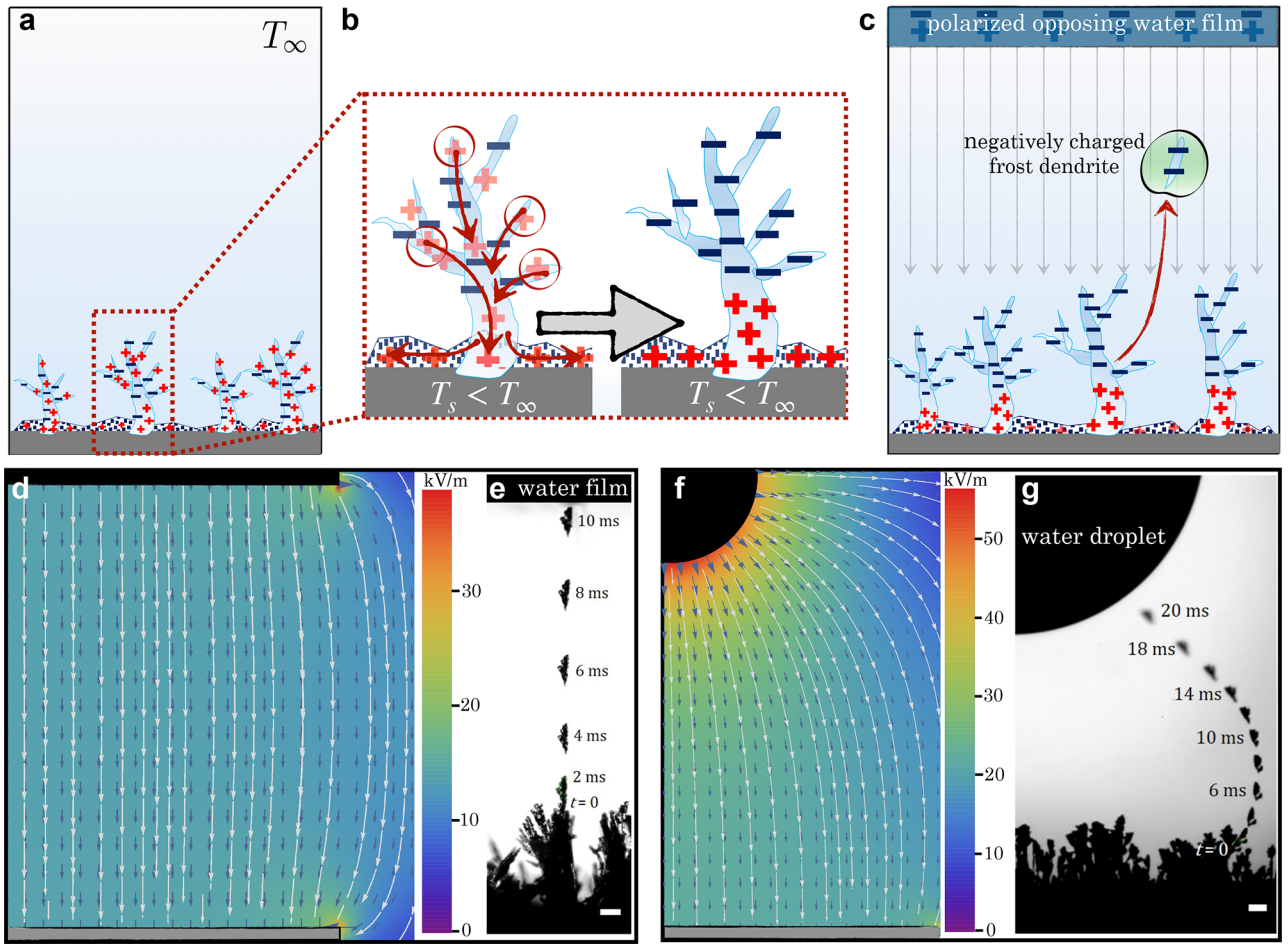

Figure 3. Origin of the attractive force on the frost dendrites. (a) Initial (nanoscale) frost exhibits a roughly uniform temperature and distribution of ions (defects) within the dendrites. (b) As the frost dendrites grow to a microscale, $T_\infty > T_s$, such that ions are more concentrated in the warmer upper dendrites. Positive ions then diffuse to the lower concentration basal frost at a much higher mobility than the negative ions. (c) This charge separation enables the fracture and jumping of frost in the presence of an opposing polarizable liquid. (d) Numerical simulation showing that, when the frost and opposing water film are both planar, the electric field is uniform. (e) This results in a straight trajectory and constant terminal velocity for jumping frost particles, validated here by chronophotography, where the particle consistently travels ~300 μm every 2 ms at terminal velocity to cross the 2.5 mm gap. (f) Numerical simulation showing that, when frost is now opposite a pendant droplet (*i.e.*, plate and sphere configuration), the electric field is nonuniform with curved field lines. (g) Chronophotography (successive position of the dendrite temporally separated by 2 ms) confirms a curved trajectory for a jumped dendrite opposite a water droplet, where the sudden increase in acceleration near the droplet is confirmed by increased distance between successive positions. Both scale bars represent 100 μm.

2d). Typical to the motion of an object in a fluid, the velocity of the frost increased continuously and then attained a terminal velocity mid-jump before reaching the wetted paper. A force balance on the jumped frost particle of mass m and velocity $v(t)$ yields $m\frac{dv(t)}{dt} = F_a - F_g - F_d$, where F_a is the attractive force between the dendrite and the water, F_g is the force of gravity, and F_d is the drag force (Figure 2d, inset). By approximating the jumping dendrite as a perfect sphere of radius R, we can assume a Stokes drag of $F_d = 6\pi\mu Rv(t)$, where μ is the viscosity of the air. The area of the real-life dendrite was approximated as its projected area, $A \approx lw$, where l and w are the in-plane length and width, and it is assumed that the dendrite is very thin. This same surface area was then mapped onto a perfect sphere to extract the effective sphere radius (R). The assumption of Stokes drag is supported by the micrometric radius of a typical jumping dendrite ($R \approx 10$ μm), such that the maximum Reynolds number of the vapor flow around the jumping dendrite is only $\mathrm{Re} = \rho V_{max}(2R)/\mu \approx$ 1.2, where $\rho = 1.2$ kg m^{-3} and $\mu = 18$ μPa s are the air density and dynamic viscosity, respectively. The maximum observed velocity of the jumped dendrites V_{max} among all trials is about 0.9 m s^{-1}. Solving the force balance for $v(t)$, with the initial condition of $v(0) = 0$, we obtain

$$v(t) = V_t[1 - e^{-t/\tau_c}] \quad (1)$$

where $V_t = (F_a - mg)/(6\pi\mu R)$ is the terminal jumping velocity and $\tau_c = m/(6\pi\mu R) = 2R^2\rho_i/9\mu$ is the characteristic relaxation time for reaching terminal velocity, with ρ_i being the density of ice. If the time to reach the water film, τ_e, is longer than τ_c, the velocity of the dendrites will reach a steady velocity. This was always the case for $H = 2.5$ and 5 mm, whereas for $H = 1$ mm a steady velocity was only reached for the smallest particle sizes (due to the R^2 dependence of τ_c). We can now nondimensionalize the experimental time with τ_c and the velocities with the corresponding experimental steady velocity for all the experiments where the dendrites reached a steady velocity. Figure 2e shows all the nondimensional experimental data collapsed over

https://dx.doi.org/10.1021/acsnano.0c09153
ACS Nano 2021, 15, 4669−4677

the theoretical curve from eq 1. We can thus use the experimentally measured values of V_t to extract F_a. For a typical case of particle radius $R \approx 10\ \mu$m, $\rho_i = 917$ kg m^{-3}, $\mu \approx 18\ \mu$Pa s, and $V_t \approx 0.1-0.9$ m s^{-1} we obtain an order of magnitude estimate for the attractive force $F_a \approx 10^{-10}-10^{-9}$ N. But now we need to understand the mechanistic origins for this attractive force.

Charge Separation in Ice: Temperature Gradient Theory. Informed by previous reports of charge separation occurring in bodies of ice that exhibit a temperature gradient,[4−6] we hypothesize that the attractive force is electrostatic in nature. This hypothesis was tested by suspending a wide variety of polar *vs* nonpolar liquids above the frost sheet (see Figure S3 and Movie 2). The jumping frost effect was consistently observed when dangling a pendant drop of a polar liquid—water, acetone, or ethylene glycol—over the frost sheet. In contrast, no jumping frost was ever observed when suspending nonpolar droplets of decane or hexadecane. Similarly, no frost dendrites fractured or propelled from the surface when using dry filter paper (or not suspending any object at all). While electrostatic charge can develop in polar liquids flowing through a channel due to the streaming current phenomenon,[16] this was not the primary mechanism in our case. The flow-independent electrification of our system was validated by two separate observations: jumping was observed when using static pendant droplets or by gently submerging the filter paper in water (rather than using a syringe pump). Triboelectric charging of the filter paper can also be neglected, as dry filter paper did not promote frost jumping. Cumulatively, these observations strongly indicate that the frost exhibits a charge separation that in turn polarizes the opposing liquid to produce an electrostatic attractive force.

The spontaneous electrification of ice has been studied intensively and almost exclusively by the atmospheric community to understand thunderstorms, especially in the mid-twentieth century.[4−6,8,17,18] The electrical state of chemically pure ice is dominated by its intrinsic charge-carrying defects: ionic defects H_3O^+ and OH^- (denoted by q and m) and reorientational Bjerrum D (positive) and L (negative) defects (d and l),[19−22] all of which are formed spontaneously by thermal activation. The thermoelectric theory put forward by Latham and Mason[5] described a temperature-gradient-induced charge separation in an ice slab. The warmer end of the ice will have a higher concentration of thermally activated ionic defects, prompting their diffusion toward the colder end. As H_3O^+ diffuses about 3.3 times faster than OH^-, this creates a potential difference across the ice with the warm and cold ends exhibiting net negative and positive charges, respectively.[6]

Let us now apply the Latham and Mason theory of charge separation to our specific case of a dendritic frost sheet grown in warm air. Upon the earliest nucleation of nanoscale frost, the temperature gradient is negligible such that the ionic defects are evenly distributed (Figure 3a). As the dendrites continue to grow outward from the nanoscale frost, their top ends will increasingly warm (eventually approaching the melting temperature), while the base of the frost is maintained at the temperature of the chilled substrate. As a result, the upper portion of the frost will become negatively charged while the basal frost becomes positively charged (Figure 3b). To validate that the charge separation in frost was required for dendrites to become attracted to the opposing water, we performed a control experiment with an isothermal frost sheet in a walk-in freezer (see Figure S2a and Movie 3). As expected, when the frost lacked an appreciable temperature gradient, the jumping effect was suppressed even when holding water over the frost. To apply our numerical model, we crudely approximate a three-dimensional frost sheet as an ice slab of thickness h (Figure 2a). The negative surface charge density on the vapor side of the frost sheet can now be estimated from the modified Latham and Mason model:[5]

$$\sigma_s = -\frac{\epsilon_r \epsilon_0 k_B}{2e}\left(\frac{u^+/u^- - 1}{u^+/u^- + 1}\right)\left(\frac{\phi_e}{k_B T} + 1\right)\frac{\Delta T}{h}\ \mathrm{C/m^2} \quad (2)$$

where $\epsilon_r = 100$ is the relative permittivity of ice, k_B is the Boltzmann constant, $\phi_e = 1.08$ eV is the activation energy to create H_3O^+ and OH^- ions in ice,[22] e is the elementary charge, $\frac{\Delta T}{h} \approx \frac{dT}{dX}$ is the temperature gradient across frost of thickness $h = 100\ \mu$m, and u represents the mobility of the ions within ice where the + and − superscripts denote H_3O^+ and OH^- ions, respectively. In general, the H_3O^+ ions are more mobile than the OH^- ions and the mobility ratio u^+/u^- is about 3.3.[22] For the average dendrite temperature T, we can use the average of the equilibrium ice−water interface temperature ($T_i \approx 0$ °C) and the substrate temperature ($T_s = -10$ °C).[23] The total change in temperature across the frost is approximated by $\Delta T \approx T_i - T_s \approx 10$ °C. With the temperature gradient $\approx 10/10^{-4} = 10^5$ K m^{-1}, the surface charge density on the frost plate is found to be $\sigma_s = -9.86 \times 10^{-8} \sim 10^{-7}$ C m^{-2}.

Origin of the Attractive Force on the Frost. These negative charges on the upper frost induce positive charges on the nearest polarizable surface, *i.e.*, the opposing water. Of course, there will be an equal amount of negative charges within the water film that will be reoriented away from the frost plate. Thus, an external electric field is set up between the frosted surface and the opposing water surface (Figure 3c). A broken piece of frost carrying a negative surface charge[7] will move upward, as this corresponds to the opposite direction of the electric field. As the relative dielectric permittivity of water is much higher than the surrounding medium ($\epsilon_{water} \approx 80$, $\epsilon_{air} \approx 1$), the internal electric field can be neglected and we can treat the water film (droplet) as a conducting plate (sphere) with positive surface charges[24] (see Figure S4a,b and Section 2.1 in the Supporting Information).

The case of a frosted surface and an opposing water film (Figure 3d) can be compared with a parallel plate capacitor, as the plate areas (~100 mm^2) are larger than the spacing between them ($H \approx 1$ mm). A uniform field of strength $E = \sigma_s/\epsilon_0 \approx 10^4$ V m^{-1} was found from subsequent analysis (Figure 3d). The charge q_f on a frost dendrite broken off the frost is found to be in the range of $10^{-14}-10^{-13}$ C from the electrostatic force equation, $F_a = q_f E$ where $F_a = 10^{-10}-10^{-9}$ N as found previously. We avoided any experimental setup to directly measure this charge on frost dendrite, as the measurement process would have likely induced error due to the temperature gradient and humidity in the vicinity of our frosted surface.[25] But previous reports on fragmented frost dendrites have reported a similar amount of charge from direct measurement, which gives us enough confidence in our minimal model.[8,12] The uniform electric field lines between the substrate and the film explains the experimental observation of the straight path of the jumped dendrite (Figure 3e). For the case of an opposing water droplet in place of a water film, we simulated the electric field by solving Laplace's equation in the space between the substrate and the droplet (see Section 2.2 in the Supporting Information). The

https://dx.doi.org/10.1021/acsnano.0c09153
ACS Nano 2021, 15, 4669−4677

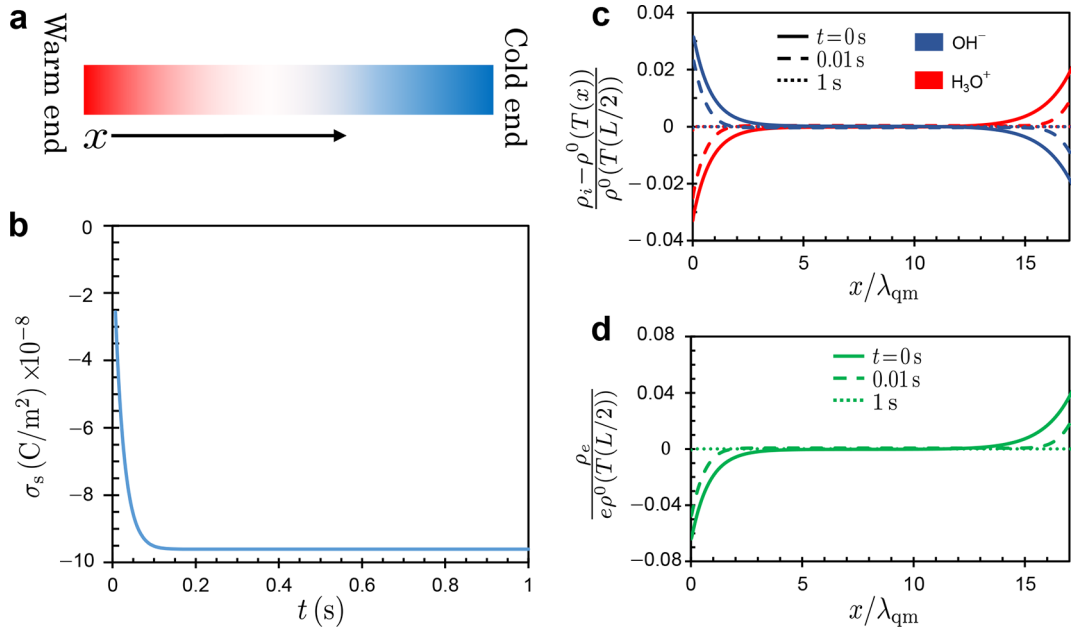

Figure 4. Numerical simulation for charge separation in an ice slab. (a) One-dimensional ice slab model with the temperature decreasing linearly from the left to the right end. The positive *x*-axis is along the direction of decreasing temperature. (b) Temporal variation of charge density in the slab's warmer left half, due to the mismatch in mobility of the OH^- and H_3O^+ ions. The negative sign of the charge density shows that the negative charges accumulate on the warmer end of the ice. The steady-state value of the surface charge density is very close to the value obtained from Latham and Mason's original formula. (c) Spatial distribution of the nonequilibrium density of OH^- and H_3O^+ ions at representative times. (d) Spatial distribution of space charge density of the ionic defects at representative times.

simulation results are shown in Figure 3f, which shows that the electric field is nonuniform and increases as we go near the droplet. Moreover, the field lines curve into the water droplet at a right angle following the rule that flux is perpendicular to the surface. This matches with our experimental observation of the curved droplet trajectory in Figure 3g and the increased acceleration of the dendrite near the droplet (see Figure S4c and Movie 4). The numerically simulated electric field values also match with the results achieved through simpler scaling analysis (see Section 2.3 in the Supporting Information).

Charge Separation in Ice: Numerical Simulation. At this point, it is important to generalize this charge separation theory for the case of an entire frost dendrite breaking off from the surface (Figure 1b). Generally, the three-dimensional frost dendrites do not grow directly on the surface but over an icy basal layer, which can be discontinuous or continuous, depending on the wettability of the substrate. Since a temperature gradient is the primary driving force of the frost jumping, the ambipolar transport of the ionic defects happens between the surfaces having the largest temperature difference, *i.e.*, between the icy layer contacting the surface and the frost–air interface. This way even an entire dendrite can carry a negative charge while the positive charges stay in the basal layer. The schematic of Figure 3a–c shows this progression of events from the frost growth until the jumping.

To complete our understanding of charge separation in ice due to a temperature gradient, a numerical simulation approach to eq 2 is presented here, for a column of ice with the same $h = 100\ \mu$m thickness, denoted as domain length (L = 100 μm), and temperature decreasing linearly from the left side to the right side (Figure 4a). Without any temperature gradient, there is a balance of H_3O^+–OH^- ions in the bulk ice, whose equilibrium is maintained by the mass action law:

$$\rho_m \rho_q = \rho^0(T)^2 \tag{3}$$

where ρ_i is the density (or concentration) of ion i in the ice slab, with i = m and q for the OH^- and H_3O^+ ions, respectively. $\rho^0(T) = \rho_m^0(T) = \rho_q^0(T) = Ne^{-\phi_e/(2k_BT)}$ is the temperature-dependent equilibrium density of the OH^- and H_3O^+ ions. $N = 3 \times 10^{28}$ m^{-3} is the concentration of oxygen molecules in ice and $\phi_e \approx 1.08$ eV is the activation energy for the ions. Although the mass action law is strictly valid only in thermal equilibrium, as a quasi-equilibrium is maintained in the ice in the presence of the thermoelectric effect, the mass action law still holds locally across the entire ice slab.

Once a small temperature gradient is induced in the slab (decreasing from left to right side of the slab), accompanying concentration gradients of H_3O^+ and OH^- ions appear in the slab. These gradients lead to the diffusive movement of H_3O^+ and OH^- ions. Due to the higher mobility of H_3O^+ ions, charge separation occurs within the ice slab with H_3O^+ (OH^-) ions enriched at ice slab's colder (warmer) side. This in turn sets up an internal ambipolar electric field that opposes the movement of the H_3O^+ ions. Eventually, the balance of electric field-driven transport and diffusion transport leads to a steady-state potential with no net current flow. The ambipolar electric field can be derived at the steady state.[26] The governing equations for the spatiotemporal variation in the ion concentrations are

$$\frac{\partial \rho_m}{\partial t} = \frac{\partial}{\partial x}\left[D_m \frac{\partial \rho_m}{\partial x} + \mu_m \rho_m E\right] + \frac{\rho_m^0(T)}{\tau_{mq}} - \frac{\rho_m \rho_q}{\rho_m^0(T)\tau_{mq}} \tag{4}$$

$$\frac{\partial \rho_q}{\partial t} = \frac{\partial}{\partial x}\left[D_q \frac{\partial \rho_q}{\partial x} - \mu_q \rho_q E\right] + \frac{\rho_q^0(T)}{\tau_{mq}} - \frac{\rho_m \rho_q}{\rho_q^0(T)\tau_{mq}} \tag{5}$$

https://dx.doi.org/10.1021/acsnano.0c09153
ACS Nano 2021, 15, 4669–4677

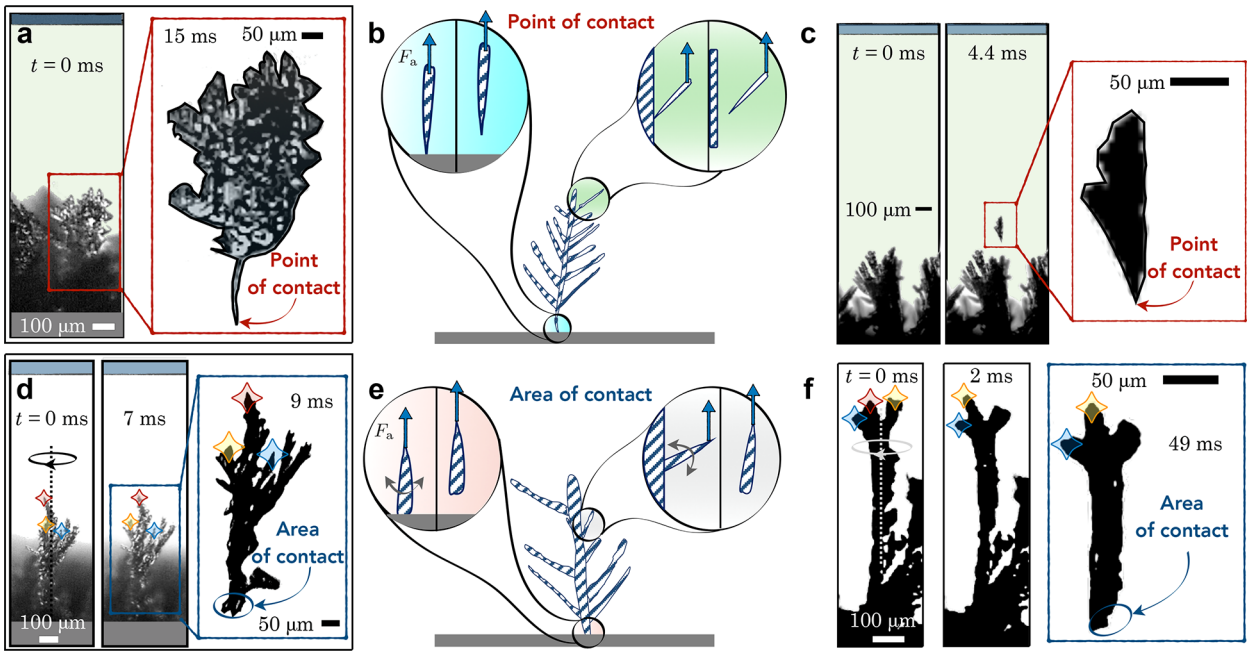

Figure 5. Mechanisms of frost break-off. (a) For a submicron point of attachment with the substrate, frost break-off occurs seemingly instantaneously. (b) Schematic showing how the point-break fracture of a dendrite can occur either from the substrate or from the "mother" frost. (c) Point-break frost detachment from the mother frost. (d) Area fracture (*i.e.*, microscale attachment length scale) of a dendrite from the substrate. The twisting motion of the dendrite is evident from the change in positions of the three branches (yellow, red, and blue colored) in the first two frames. The axis and direction of rotation are shown to help in the visualization. It takes about 7 ms from the beginning of the twisting motions to the completion of crack propagation and break-off. (e) Schematic showing the twisting and/or turning motion before the complete fracture of a dendrite from either the substrate or the mother frost. (f) Area fracture from the mother frost. $t = 0$ denotes the start of movement for the dendrite. At $t = 2$ ms, the yellow and blue dotted branches can be seen at a different location, while the branch with the red dot has moved into the page and is obscured from the viewer. All zoomed-in photographs in (a), (c), (d), and (f) show the full shape of the detached frost midflight, with a digital outline for visual clarity. The snapshots are from Movie 5.

$$\frac{\partial E}{\partial x} = \frac{e(\rho_q - \rho_m)}{\epsilon_0 \epsilon_r} \tag{6}$$

where $\mu_m \approx 3 \times 10^{-8}$ m^2 V^{-1} s^{-1} and $\mu_q \approx 10^{-7}$ m^2 V^{-1} s^{-1} are the mobility of the OH^- and H_3O^+ ions, respectively, E is the intensity of the electric field set up by the space charge, e is the elementary charge, $\epsilon_r = 100$ is the relative dielectric permittivity of ice, and $\tau_{mq} = 2 \times 10^{-5}$ s is the recombination time for the ions.[22] The first two terms on the right side of eqs 4 and 5 are simply Fick's law and Ohm's law, respectively, describing the contribution of ion concentration and internal electric field on the transport of ions. As both of these processes are related, the coefficients of the first two terms are also related by the Einstein relation $D_{m,q} = \mu_{m,q} k_B T/e$. Although these were present in the original Latham and Mason model, a more general model of ion balance in ice should also include volumetric source terms.[27] The last two terms in eqs 4 and 5 account for the generation and annihilation (or recombination) of ions, respectively, following the mass action law. Together they constitute the volumetric source term or the net charge produced within the ice.

These equations can now be solved simultaneously, with the following boundary conditions defined at the left and right side of the ice slab:

$$J_m(0) = J_m(L) = 0 \tag{7}$$

$$J_q(0) = J_q(L) = 0 \tag{8}$$

$$E(0) = E(L) = 0 \tag{9}$$

where the fluxes of the OH^- and H_3O^+ ions are depicted by $J_m(x) = -D_m \frac{\partial \rho_m}{\partial x} - \mu_m \rho_m \cdot E$ and $J_q(x) = -D_q \frac{\partial \rho_q}{\partial x} + \mu_q \rho_q E$. At $t = 0$, OH^- and H_3O^+ ions are in their local equilibriums with $\rho_m{}^0(x) = \rho_q{}^0(x) = Ne^{-\phi_e/(2k_B T(x))}$.

Figure 4b shows the evolution of the net charge of OH^- and H_3O^+ ions in the left half of the ice. We can see that the net charge density reaches a steady state, $\sigma_s = 9.6 \times 10^{-8}$ C m^{-2}, after about 0.1 s. This is very close to the value $\sigma_s = 9.86 \times 10^{-8}$ C m^{-2} we got using the original Mason's formula. The small difference is caused by the fact that, unlike Mason's model, we have not considered the thermally driven transport of the OH^- and H_3O^+ ions in eqs 4 and 5. The negative sign on the accumulated charge on the warmer left-hand side of the ice slab confirms the temperature gradient-induced charge separation process in ice where the warmer end accumulates a net negative charge. The spatial distribution of the concentration of these ionic defects and net charge density is also shown at some representative times (Figure 4c,d). In Figure 4c, the nonequilibrium density of the ionic defects, $\rho_i - \rho^0(T(x))$, is nondimensionalized by the equilibrium density of the ions at the middle of the ice slab, $\rho^0(T(x = L/2))$, which is the same for OH^- and H_3O^+ ions. The spatial distance is nondimensionalized by the Debye length of the ionic defects, $\lambda_{qm} = \sqrt{\epsilon_0 \epsilon_r k_B T/2\rho^0 e^2}$. The charge separation only happens within a few Debye length distance in each end, while the bulk region remains neutral. In Figure 4d, the spatial variation of the

https://dx.doi.org/10.1021/acsnano.0c09153
ACS Nano 2021, 15, 4669−4677

space charge density, $\rho_e = e(\rho_q - \rho_m)$, is plotted for different times, which shows the concept of Debye length clearly.

Latham and Mason's model for charge separation in ice,[5] adapted here to estimate the surface charge density, did not consider the effect of Bjerrum defects. This may seem a curious omission, considering that Bjerrum defects are 10^4–10^6 times more abundant than ionic defects. However, attempts to include Bjerrum defects in our thermal migration model (as well as attempts by others)[27] resulted in a positive charge on the warmer end of the frost when commonly used thermodynamic and transport properties of these defects were adopted in the model. This contradicts clear experimental evidence of the frost splinters exhibiting a negative charge, validated by using charged copper electrodes (Figure S5) and measured directly by others.[7−9] We hypothesize that the Bjerrum defects do not appreciably contribute to the charge separation because the preferential top-to-bottom thermal migration of negative L defects is largely canceled out by the migration of positive D defects from the outer surface of the frost to the interior, as suggested by recent density functional theory simulations (see Section 3 of the Supporting Information).[28] We hope that this report will inspire further research on the effect of migrating Bjerrum defects on charge separation and electrostatic ice removal. It would also be interesting to vary the ambient gas phase and/or humidity, which was beyond the scope of this initial study. Higher humidity causes faster frost growth, which in turn can affect the charge separation process in the frost layer. The impurities in the ambient gas can also affect the charge on the outer frost layer.[3]

Fracture of a Frost Dendrite from the Frost Sheet. The last piece of the puzzle is the fracturing of the frost dendrites, from either the substrate or "mother" frost, which is a prerequisite for the subsequent jumping. High-speed microscopy indicates two distinct modes of fracture. In one mode, the area where fracture occurs is approaching a point contact ($l_a \lesssim 1$ μm length scale), such that breakage occurs instantaneously with respect to the temporal resolution of the high-speed video (Figure 5a−c). In contrast, when the length scale of attachment is more than $l_a \gtrsim 10$ μm, the dendrite(s) twists and turns before complete breakage (Figure 5d−f). We hypothesize that these two seemingly different mechanisms of fracture are related by the rate of crack propagation in ice. Although finding the exact crack propagation rate in ice under tensile stress requires the precise knowledge of its grain structures, here we use scaling analysis to capture the physics.

From the Griffith condition for crack initiation, the nucleating crack length r_0 can be found by equating the attractive force with the crack initiation force,[29,30]

$$F_a = \pi {r_0}^2 \sqrt{\frac{8Ew_{ad}}{(1-\nu^2)\pi r_0}} \tag{10}$$

where $E = 8.7$ GPa is the modulus of elasticity of ice, $w_{ad} \approx 2\gamma_{i,a} = 0.2$ J m^{-2} is the work of adhesion inherent to creating an ice−air double interface, and $\nu = 0.31$ is Poisson's ratio for ice. Using our previously obtained scaling estimate of $F_a = 10^{-10}$–10^{-9} N in eq 10, the nucleating crack length can be solved as $r_0 \approx 10^{-10}$ m. We can then express the overall stress intensity factor, assuming the tensile loading of an edge crack of length r_0, as $K_I \approx \sigma_\infty \sqrt{\pi r_0}$, where $\sigma_\infty = F_a/\pi {l_a}^2$ is the applied stress.[31] The maximum applied stress due to the maximum force $F_a = 10^{-9}$ N is $\sigma_\infty \approx 10^4$ Pa for a submicron contact point ($l_a \approx 100$ nm) and $\sigma_\infty \approx 1$ Pa for a micron-sized area of contact ($l_a \approx 10$ μm). This translates to stress intensity factors of $K_I \approx 1$ Pa m$^{1/2}$ and 10^{-4} Pa m$^{1/2}$, respectively, far less than the fracture toughness of ice, $K_{Ic} = 10^5$ Pa m$^{1/2}$. We will therefore assume a subcritical crack growth velocity, which for brittle materials tends to scale as $v_c \approx 1$ mm s^{-1}.[32] For such a crack to propagate and completely detach the dendrite from the substrate or the "mother" frost, it would take about $l_a/v_c \approx 10^{-7}/10^{-3} \approx 100$ μs for a 100 nm attachment (Figure 5a,c) and about $l_a/v_c \approx 10^{-5}/10^{-3} \approx 10$ ms for a 10 μm contact length (Figure 5d,f). The experimental videos were recorded at ∼10 kHz (100 μs per frame), such that the temporal resolution was approximately equal to the crack propagation time for the case of a 100 nm attachment. This explains why complete detachment appears to be instantaneous in the case of submicron attachments. In contrast, crack propagation along a 10 μm contact length would require ∼100 frames to complete, which is what enabled the visualization of the twisting and turning motions prior to detachment. This scaling estimate for the crack propagation time matches with our experimental observations, where 440 frames (averaged across three trials) were required from the initiation of twisting and turning to the complete detachment of $l_a \approx 10$ μm attachments prior to jumping.

CONCLUSIONS

While the spontaneous charging of growing ice particles has been studied by atmospheric physicists to understand cloud electrification during a thunderstorm,[7,17,33] the analogous charge separation of frost growing on substrates has been largely ignored by surface scientists. Here, we reported that micrometric frost growing on a chilled surface can dramatically fracture and jump into the air in the presence of polarizable liquids. Our experiments and analysis, correlated with Latham and Mason's classical model, revealed that such motion results from the temperature-gradient-induced charge separation within a growing layer of frost and consequent electrical attraction by the opposing liquid. Our simple approach of correlating the high-speed imaging of jumping ice particles with a dynamical model allows for the controlled laboratory study of charge separation in ice, which may help atmospheric physicists to better understand thunderstorm electrification. Conversely, the findings described here could be stepping stones for the development of an electrostatic deicing technique, where we envisage that high-voltage electrodes could replace the water film to propel larger masses of ice from their substrate.

MATERIALS AND METHODS

Experiments in a Room-Temperature Environment. The basic experimental setup for the jumping frost experiments in the laboratory ambient condition is shown in Figure S1a. A Peltier stage was fixed to a goniometer stage (Ramé-Hart, model 590) used for growing frost on different substrates. The default needle assembly with stainless steel needles (inner and outer diameters of 0.7 and 2.1 mm, respectively) was used to hold pendant droplets of water or other liquids over the frost sheet. The droplet volume was varied between 1 and 10 μL by using a syringe pump (Ramé-Hart, model 100-22). Slight modifications were done to this existing setup to hold a thin water film opposite the frosted substrates. A piece of filter paper (Sartorius) was attached with glue to the underside of a 3D-printed holder (Figure S1b). The plastic tube attached to the holder ensured proper fitting with the needle assembly. The syringe pump supplied about 100 μL of water to the filter paper through the needle assembly

https://dx.doi.org/10.1021/acsnano.0c09153
ACS Nano 2021, 15, 4669−4677

and the hollow channel. The experiments were recorded from the side with a high-speed camera (Vision Research, Phantom v711) attached to a macrolens (Canon MP-E 65 mm f/2.8 1−5×).

Experiments under Isothermal Conditions. Frost was grown on a hydrophobic silicon wafer (T_s = −10 °C) in the docking room (T_∞ = 3.2 °C, RH = 73.6%) of a walk-in freezer (T_∞ = −12.7 ± 0.3 °C, RH = 72.6 ± 3%). The relative humidity and temperature of the freezer were measured using a humidity and temperature probe (E+E Elektronik, model EE210). Once the silicon substrate was evenly covered with frost, it was quickly brought into the freezer and left for 10 min before running experiments, to ensure that the frosted surface reached the same temperature as the freezer. Room-temperature water and the 3D-printed filter paper holder were brought into the freezer prior to the experiment, to similarly ensure that they cooled to the freezer's air temperature. Just before the experiment, the filter paper was touched gently on the surface of the supercooled water to create a film of water and then held over the frosted surface. No jumping was observed over a ∼5 min span for each of the three trials. In Figure S2a, we have included results of one such trial, where two frames are separated by 160 ms without any jumping in-between them.

Effect of Air Flow on the Jumping. A point of concern for the jumping frost experiments was whether air currents could affect the phenomenon. We addressed this issue in two different ways. First, an anemometer with a minimum resolution of 0.3 m s^{-1} (Omega, model HHF81) consistently output a zero value when held near the experimental setup, confirming that no substantive air flow was present. While it is inevitable that the chilled substrate held within a room-temperature ambient will induce natural convection, we note that the convective current would be moving toward the substrate, in the opposite direction of the jumping frost. Second, a supplemental series of experiments were conducted within a closed Peltier environmental chamber (Ramé-Hart, model P/N 100-30, dimensions: 81 × 55 × 44 mm), where the jumping phenomenon was similarly observed (Figure S2b). These findings cumulatively indicate that the jumping frost phenomenon was not appreciably affected by convective currents for our experiments.

Effect of the Substrates and the Opposing Liquids on the Jumping. For all of the experiments reported here, we used hydrophobic silicon wafers to grow frost. Untreated hydrophilic glass and superhydrophilic aluminum were also attempted, all of which exhibited the same jumping frost phenomenon (Figure S2b,c). This indicates that the jumping frost phenomenon can occur on substrates where wettability, electrical conductivity, and thermal conductivity widely vary. However, we do expect that the hydrophilic surface will exhibit a higher frequency of frost dendrites from the ice−substrate interface (as opposed to breaking off from the mother frost) because of the reduced ice adhesion strength.[34] On the hydrophilic and superhydrophobic substrate, the dendritic frost growth was preceded by the freezing of supercooled filmwise condensation.[35] As this is not fundamentally different from growing frost from an ice sheet, we believe that the same jumping frost effect would have been observed if the substrate was initially covered in ice.

Water droplets and films were used in most of the experiments, but additional liquids such as acetone, ethylene glycol, and decane were also used. For acetone and ethylene glycol, which are both polar due to the presence of more electronegative oxygen atoms, jumping dendrites were observed similar to the case of water (Figure S3a,b). When a thin film of decane, a hydrocarbon, was used as the opposing liquid, no jumping was observed for as long as 5 min (Figure S3c).

Image Processing. An open-source software (Tracker) was used to track the jumped icicles over time and obtain the velocity *vs* time plot shown in Figure 2d. For each case, t = 0 is chosen as the frame preceding the complete breakage of a frost dendrite. The origin of the coordinate system was placed at the point of contact of the jumping icicle with the substrate or the mother frost.

ASSOCIATED CONTENT

Supporting Information

The Supporting Information is available free of charge at https://pubs.acs.org/doi/10.1021/acsnano.0c09153.

Figures S1−S5: effect of the air gap height on the frequency of jumping frost, details of electric field simulation, effect of Bjerrum defects, and captions for Movies 1−5 (PDF)
Supplementary video (MP4)
Supplementary video (MP4)
Supplementary video (MP4)
Supplementary video (MP4)
Supplementary video (MP4)

AUTHOR INFORMATION

Corresponding Author

Jonathan B. Boreyko − *Department of Mechanical Engineering, Virginia Tech, Blacksburg, Virginia 24061, United States;* orcid.org/0000-0003-0344-5868; Email: boreyko@vt.edu

Authors

Ranit Mukherjee − *Department of Biomedical Engineering and Mechanics, Virginia Tech, Blacksburg, Virginia 24061, United States*

S. Farzad Ahmadi − *Department of Mechanical Engineering, Virginia Tech, Blacksburg, Virginia 24061, United States; Department of Mechanical Engineering, University of California Santa Barbara, Santa Barbara, California 93106, United States;* orcid.org/0000-0001-8622-1434

Hongwei Zhang − *Department of Mechanical Engineering, Virginia Tech, Blacksburg, Virginia 24061, United States*

Rui Qiao − *Department of Mechanical Engineering, Virginia Tech, Blacksburg, Virginia 24061, United States;* orcid.org/0000-0001-5219-5530

Complete contact information is available at: https://pubs.acs.org/10.1021/acsnano.0c09153

Author Contributions

S.F.A. discovered the jumping frost phenomenon. S.F.A. and J.B.B. conceived the research. R.M. and S.F.A. designed and carried out the experiments in the laboratory and walk-in freezer. R.M. and S.F.A. analyzed the data. H.Z. and R.Q. performed the numerical analysis. R.M., S.F.A., H.Z., R.Q., and J.B.B. developed the theoretical analysis. R.M., S.F.A., and J.B.B. prepared the manuscript. All authors proofread the paper, made comments, and approved the manuscript.

Notes

The authors declare no competing financial interest.

ACKNOWLEDGMENTS

This work was supported by the National Science Foundation (CBET-2034242). The authors thank P. Shukla for the design and fabrication of the 3D-printed paper holder. Special thanks to K. Nimmakayala, H. Park, and S. Propst for their help with the walk-in freezer experiments. We are also grateful to R. Clarkson, L. Crook, J. Cummings, C. Son, and S. Nath for fruitful discussions.

REFERENCES

(1) Brindle, I.; Tomlinson, R. Deflection of Falling Solvents by an Electric Field. *J. Chem. Educ.* **1975**, *52*, 382−383.

(2) Su, X.; Lianos, L.; Shen, Y. R.; Somorjai, G. A. Surface-Induced Ferroelectric Ice on Pt(111). *Phys. Rev. Lett.* **1998**, *80*, 1533−1536.
(3) Takahashi, T. Electrification of Growing Ice Crystals. *J. Atmos. Sci.* **1973**, *30*, 1220−1224.
(4) Workman, E. J.; Reynolds, S. E. Electrical Phenomena Occurring during the Freezing of Dilute Aqueous Solutions and Their Possible Relationship to Thunderstorm Electricity. *Phys. Rev.* **1950**, *78*, 254−260.
(5) Latham, J.; Mason, B. J. Electric Charge Transfer Associated with Temperature Gradients in Ice. *Proc. R. Soc. London A* **1961**, *260*, 523−536.
(6) Jaccard, C. Thermoelectric Effects in Ice Crystals: I. Theory of the Steady State. *Phys. Kondens. Materie.* **1963**, *1*, 143−151.
(7) Findeisen, W. Über die Entstehung der Gewitterelektrizität. *Meteor. Z.* **1940**, *57*, 201−215.
(8) Latham, J. The Electrification of Frost Deposits. *Q. J. R. Meteorol. Soc.* **1963**, *89*, 265−270.
(9) Dong, Y.; Hallett, J. Charge Separation by Ice and Water Drops during Growth and Evaporation. *J. Geophys. Res. Atmos.* **1992**, *97*, 20361−20371.
(10) Schaefer, V. J.; Cheng, R. J. The Production of Ice Crystal Fragments by Sublimation and Electrification. *J. Rech. Atmos.* **1971**, *5*, 5−10.
(11) Zawidzki, T. W.; Papée, H. M. Pseudo-Whiskers of Ice, Grown from Clouds of Supercooled Water in an Electric Field. *Nature* **1962**, *196*, 568−569.
(12) Bartlett, J. T.; van den Heuval, A. P.; Mason, B. J. The Growth of Ice Crystals in an Electric Field. *Z. Angew. Math. Phys.* **1963**, *14*, 599−610.
(13) Vonnegut, B. Orientation of Ice Crystals in the Electric Field of a Thunderstorm. *Weather* **1965**, *20*, 310−312.
(14) Schaefer, V. J. The Generation of Large Number of Ice Crystals in an Electric Field. *J. Appl. Meteorol. Climatol.* **1968**, *7*, 452−455.
(15) Nath, S.; Ahmadi, S. F.; Boreyko, J. B. A Review of Condensation Frosting. *Nanoscale Microscale Thermophys. Eng.* **2017**, *21*, 81−101.
(16) Xie, Y.; Bos, D.; de Vreede, L. J.; de Boer, H. L.; van der Meulen, M.; Versluis, M.; Sprenkels, A. J.; van den Berg, A.; Eijkel, J. C. T. High-Efficiency Ballistic Electrostatic Generator Using Microdroplets. *Nat. Commun.* **2014**, *5*, 3575.
(17) Mason, B. J. A Critical Examination of Theories of Charge Generation in Thunderstorms. *Tellus* **1953**, *5*, 446−460.
(18) Latham, J.; Stow, C. D. Electrification Associated with the Evaporation of Ice. *J. Atmos. Sci.* **1965**, *22*, 320−324.
(19) Pauling, L. The Structure and Entropy of Ice and of Other Crystals with Some Randomness of Atomic Arrangement. *J. Am. Chem. Soc.* **1935**, *57*, 2680−2684.
(20) Bernal, J. D.; Fowler, R. H. A Theory of Water and Ionic Solution, with Particular Reference to Hydrogen and Hydroxyl Ions. *J. Chem. Phys.* **1933**, *1*, 515−548.
(21) Bjerrum, N. Structure and Properties of Ice. *Science* **1952**, *115*, 385−390.
(22) Petrenko, V. F.; Ryzhkin, I. A. Surface States of Charge Carriers and Electrical Properties of the Surface Layer of Ice. *J. Phys. Chem. B* **1997**, *101*, 6285−6289.
(23) Libbrecht, K. G. Physical Dynamics of Ice Crystal Growth. *Annu. Rev. Mater. Res.* **2017**, *47*, 271−295.
(24) Jackson, J. D. *Classical Electrodynamics*; John Wiley & Sons: New York, 1999.
(25) Guardiola, J.; Rojo, V.; Ramos, G. Influence of Particle Size, Fluidization Velocity and Relative Humidity on Fluidized Bed Electrostatics. *J. Electrost.* **1996**, *37*, 1−20.
(26) Kapon, E. *Semiconductor Lasers I: Fundamentals*; Academic Press: Cambridge, MA, 1999.
(27) Seifert, P. A. *The Potential Difference in Ice Crystal Due to the Thermoelectric Effect*. Ph.D. thesis, North Dakota State University, 2003.
(28) Watkins, M.; VandeVondele, J.; Slater, B. Point Defects at the Ice (0001) Surface. *Proc. Natl. Acad. Sci. U. S. A.* **2010**, *107*, 12429−12434.
(29) Gao, H.; Yao, H. Shape Insensitive Optimal Adhesion of Nanoscale Fibrillar Structures. *Proc. Natl. Acad. Sci. U. S. A.* **2004**, *101*, 7851−7856.
(30) Ahmadi, S. F.; Nath, S.; Kingett, C. M.; Yue, P.; Boreyko, J. B. How Soap Bubbles Freeze. *Nat. Commun.* **2019**, *10*, 2531.
(31) Virot, E.; Ponomarenko, A.; Dehandschoewercker, E.; Quéré, D.; Clanet, C. Critical Wind Speed at Which Trees Break. *Phys. Rev. E* **2016**, *93*, 023001.
(32) Fineberg, J.; Gross, S. P.; Marder, M.; Swinney, H. L. Instability in Dynamic Fracture. *Phys. Rev. Lett.* **1991**, *67*, 457−460.
(33) Latham, J.; Mason, B. J. Generation of Electric Charge Associated with the Formation of Soft Hail in Thunderclouds. *Proc. R. Soc. London A* **1961**, *260*, 537−549.
(34) Bharathidasan, T.; Kumar, S. V.; Bobji, M. S.; Chakradhar, R. P. S.; Basu, B. J. Effect of Wettability and Surface Roughness on Ice-Adhesion Strength of Hydrophilic, Hydrophobic and Superhydrophobic Surfaces. *Appl. Surf. Sci.* **2014**, *314*, 241−250.
(35) He, M.; Wang, J.; Li, H.; Song, Y. Super-Hydrophobic Surfaces to Condensed Micro-Droplets at Temperatures Below the Freezing Point Retard Ice/Frost Formation. *Soft Matter* **2011**, *7*, 3993−4000.

https://dx.doi.org/10.1021/acsnano.0c09153
ACS Nano 2021, 15, 4669−4677